DOI: 10.13009/EUCASS2022-6177
9TH EUROPEAN CONFERENCE FOR AERONAUTICS AND SPACE SCIENCES (EUCASS)

Anomaly Detection Method of Spacecraft Propulsion Using Multiplexed Fiber Bragg Gratings

Kohji Tominaga, Go Fujii*, Taiichi Nagata*, Daichi Wada**, Shinsaku Hisada**, Kaname Kawatsu*, Tokio Kasai***
** Japan Aerospace Exploration Agency (JAXA)*
2-1-1 Sengen, Tsukuba City, Ibaraki, Japan
***Japan Aerospace Exploration Agency (JAXA)*
6-13-1 Osawa, Mitaka City, Tokyo, Japan

Abstract

This paper demonstrates the applicability of a novel anomaly detection method by multiplexed fiber Bragg gratings (FBGs). The method uses the measured external strain on piping due to water hammers. The authors found that the strain has an error of 2% at the maximum water hammer pressure and 1% at the natural frequency for the measured pressure. The FBG sensor accuracy is equivalent to that of a pressure sensor. Furthermore, it was found that anomalies could be detected by comparing the frequency response function (FRF) of any two points. Anomalies can be located in given sections by comparing FRFs.

1. Introduction

Pressure sensing technology is important to understand the integrity of spacecraft propulsion systems. As these systems become more sophisticated, their safety and reliability requirements become even more demanding, especially for takeoffs, landings, and deep-space exploration. To meet the new challenges, we have been studying the health monitoring of propulsion systems, focusing on the dynamic pressure response during valve operation. The aim is to realize autonomous fault detection and fault diagnosis of propulsion systems with limited sensing resources [1,2]. Innovative technologies promise to improve the reliability of spacecraft propulsion systems and simplify system redundancy.

A spacecraft obtains the desired thrust by injecting and reacting high-pressure propellant in its thrusters for orbital maneuvering and attitude control. During thruster injection, the propellant valves open and close rapidly, and large pressure fluctuations occur in the supply piping. These fluctuations are called water hammer, and excessive water hammer can cause a spacecraft propulsion system to fail [3]. The maximum water hammer pressure ΔP_{max} at this time is expressed as the product of the fluid density ρ, the sound velocity c, and the velocity variation ΔV as in Equation (1).

$$\Delta \boldsymbol{P_{max}} = \boldsymbol{\rho \cdot c \cdot \Delta V} \quad \textbf{(1)}$$

Methods have been developed for health monitoring inside piping based on changes in the dynamic response of pressure by taking advantage of water hammer [1,2]. However, spacecraft propulsion systems have a minimum number of pressure sensors due to their weight and the limited number of sensor channels. Therefore, the amount of information available for health monitoring is limited.

The Fiber Bragg Grating (FBG) is a sensor that measures the strain at a certain point using the change in reflected wavelength caused by the interval changes of the diffraction grating [4]. This study examined the detection of external strain caused by a water hammer using an FBG mounted around a propulsion system pipe. Measuring the internal pressure of piping from the outside has been studied extensively in ground experiments. In addition, it has been applied widely to large structures, such as the detection of internal fluid pressure changes in nuclear plant piping [5] and the detection of surface water pressure changes on a ship's hull [6]. However, the outer diameters

DOI: 10.13009/EUCASS2022-6177

of pipes in spacecraft propulsion systems are often ½" (12.7 mm) or ¼" (6.35 mm), considerably smaller than in these examples. The measurement accuracy of the internal pressure changes by an FBG around such a narrow pipe has not been clarified.

Another feature of FBG is that multiplexing measurement is possible by inscribing many FBGs on a single optical fiber. This feature enables us to make measurements in locations where it is difficult to install pressure sensors, and to monitor the entire spacecraft propulsion system through a single channel. We focused on the sound velocity in the propellant, which is one of the dominant parameters of the dynamic response characteristics of the propellant supply system that is important from the viewpoint of stable thrust generation. We considered that it would be possible to detect an anomaly and estimate the anomalous section by comparing the correlation obtained from any two points for each condition regarding the dynamic response which may be affected by change of the sound velocity in propellant due to trapped gas. However, it is unclear what features are sensitive to anomalies and whether they enable us to estimate the anomaly intervals.

This study aims to clarify a method to detect anomalies using multiplexed FBGs with multipoint correlation. In this study, water flow tests simulating pulse propellant injection were conducted in the piping system shown in Figure 1. The pressure changes due to the water hammer generated when the solenoid valve was opened and closed were captured by the pressure sensor as the internal pressure of the piping. At the same time, the external strain of the piping was measured by the FBGs. The measured strain was converted to pressure, and the accuracy of the FBG was evaluated by comparing it with the value measured by a pressure sensor. The accuracy of the FBG measurement was also evaluated by comparing the converted pressure from the strain at the points where pressure sensors were not installed with the calculated values from the analytical model. The time and frequency characteristics of the strain-converted pressure were confirmed, and the characteristic quantities that could be used to detect faults were extracted. Furthermore, we focused on the correlation between any two points and confirmed the feasibility of fault detection and fault interval estimation.

2. Experimental and analytical methods

2.1. Outline of the water runoff test and experimental conditions

A water flow test was conducted using a simple simulation of the supply piping of a spacecraft propulsion system and pressure conditions. Figures 1(a) and 1(b) are a photograph of the test apparatus and a schematic diagram of the water piping used in this test. Deaerated pure water was used as the test fluid. After a vacuum pump evacuated the downstream system of the tank, the FCV was opened to vacuum prime the entire test system with deionized water. The internal fluid pressure before opening the solenoid valve was constantly 2.0 MPaG for each test condition. The pressure response of the internal fluid generated by the opening and closing of the solenoid valves (SV1 and SV2), which simulate propellant valves, was measured using pressure sensors, and the data were recorded using Omni-ace. At the same time, the circumferential strain of the piping due to the pressure change of the internal fluid was measured using FBGs (manufactured by Fujikura Ltd.). The test pipe from P1 to the T-junction was made of SUS and had an outside diameter of ½". SUS piping with an outside diameter of ¼" was used in the downstream section. P1 was installed downstream of the flow control valve (FCV), PIU1 was installed upstream of SV1, and PIU2 was installed upstream of SV2 (both with pressure sensors manufactured by Kyowa Dengyo in the 5 MPaG range), and the static pressure of the internal fluid was measured.

FBG1 (near P1), FBG4 (near PIU1), and FBG6 (near PIU2) were installed near each pressure sensor to measure the strain for comparison with the pressure of the pressure sensor. FBG2 (downstream of P1), FBG3 (upstream of SV1), and FBG5 (upstream of SV2) were attached to the T-junction as well to establish the feasibility of multiplexed measurement. FBG1 and 2, which were placed on the 1/2" pipe, were attached around the pipe surface and fixed using instant glue (Figure 1(a)). On the other hand, FBGs 3, 4, 5, and 6 in the 1/4" pipes were attached to the pipe surface at a 45° angle from the circumferential direction to the longitudinal direction to reduce light loss due to steep bending. The FBGs were connected by a connector and to a light source, and the output power obtained from the FBGs was measured. The measurement was monitored using a PC with LabVIEW. The changes in the measured wavelength due to pressure fluctuations were converted into strain in LabVIEW, and the strain data were obtained as a time series.

DOI: 10.13009/EUCASS2022-6177

(a)

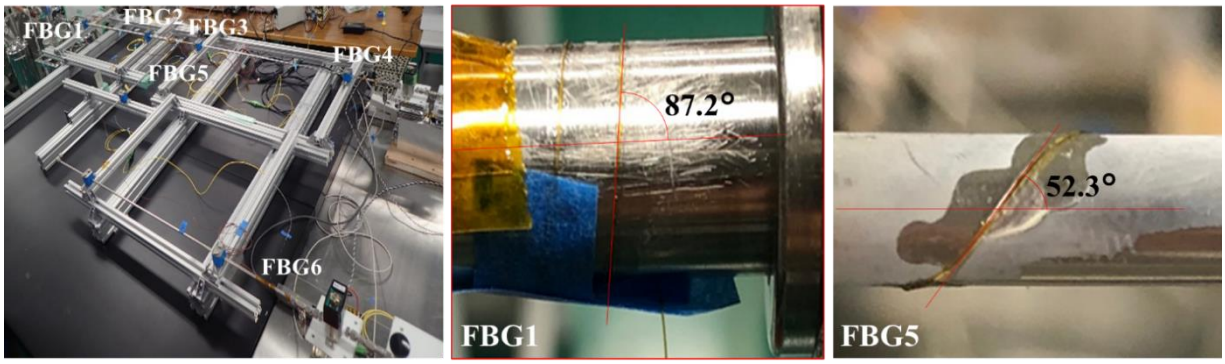

(b)

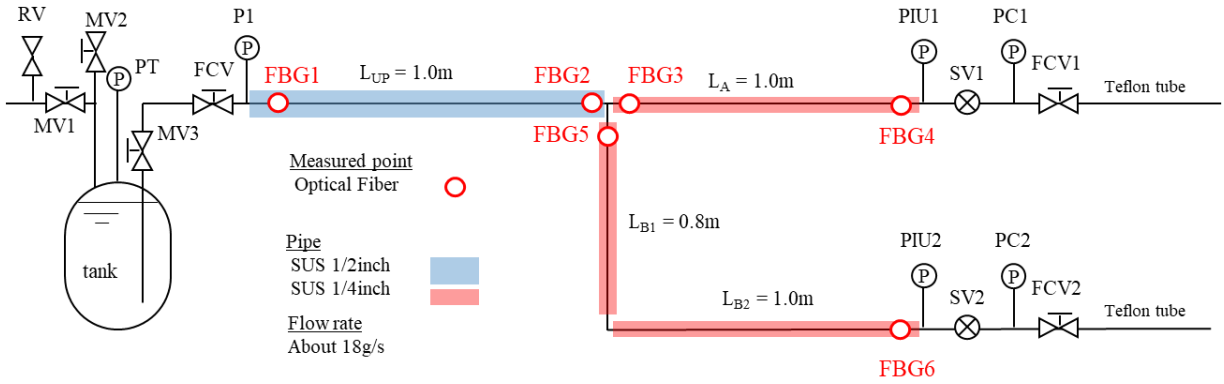

(c)

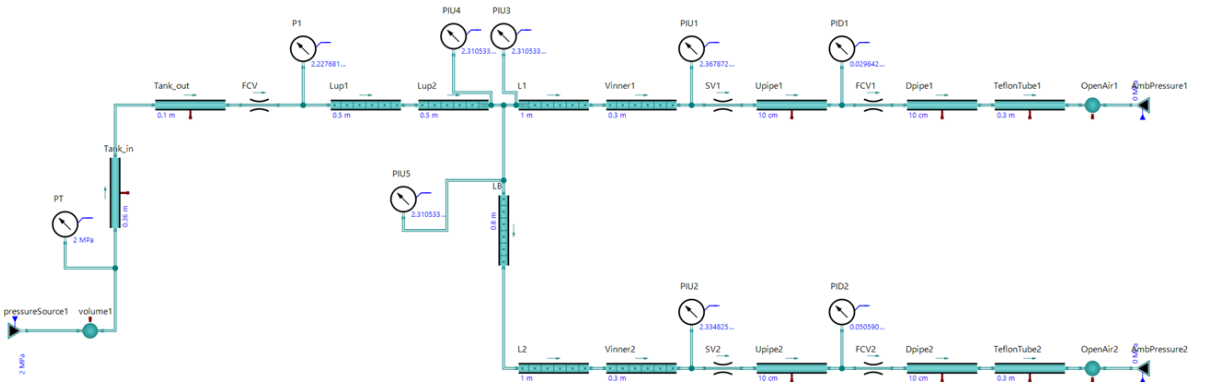

Figure 1: Water flow test system and analytical model system diagram. (a) Water flow test system overview and the FBG construction condition. (b) Schematic diagram of the water flow test system. (c) Schematic diagram of the analysis model simulating the test system

Table 1 shows the test conditions for the water flow test. The solenoid valve open/close mode was set based on the duty ratios (100 ms ON/300 ms OFF, 62 ms ON/63 ms OFF, 50 ms ON/150 ms OFF, 20 ms ON/60 ms OFF, 160 ms ON/40 ms OFF), which are the open/close time ratios commonly used in actual spacecraft thruster control. Three pulses were generated for each experimental condition. The outlet flow rate was adjusted at the downstream manual needle valves (FCV1 and FCV2) just before the start of the test to be 18.0 g/s, referring to the propellant flow rate supplied to thrusters used for spacecraft attitude control. The test modes were mode 1 (normal, Test-01), mode 2 (SV1 opening error, Test-02), mode 3 (SV2 opening error, Test-03), mode 4 (normal L part configuration change, Test-04), mode 5 (air bubble localization L part configuration change, Test-05), mode 6 (normal T-junction configuration change, Test-06), and mode 7 (air bubble localization T-junction configuration change, Test-07). Since the recording devices for the FBG and the pressure sensor are different from those for LabView and Omni-ace, respectively, the FBG strain time-series data is matched to the pressure sensor time-series data with an error of 1 ms or less.

DOI: 10.13009/EUCASS2022-6177

2.2. Model construction and analysis using 1D-CAE

Kawatsu *et al.* has been developing model-based method for spacecraft propulsion systems to evaluate performance, analyze risks, and generate before-the-fact data for health monitoring [1,2]. By using SimulationX, a complex physical quantity model analysis tool compatible with the Modelica language, the propellant tank, propellant supply piping, and valves used for flow control are modeled, and their dynamic response analysis is conducted. In this study, the water flow test system shown in Figure 1(c) was modeled using SimulationX. The tank volume and the lengths of each pipe are simulated for the test system, and the outlet of the system is a tank with a volume of $10^6 m^3$ to simulate openness to the atmosphere. The test fluid model was created by referring to various properties of water as the test fluid. The position of the pressure sensor model was set to the same as the position of the pressure sensor in the experiment. Furthermore, to simulate the FBG measurement at the T-junction section, the pressure sensor model was set at the position of FBG2, 3, and 5. The flow rate, the dominant parameter for the amplitude of water hammer pressure, was adjusted by the opening parameters of FCVs 1 and 2 as in the test system. The flow rate was set to 18.0 g/s, the same level as in the experiment. The solenoid valve opening/closing time was also set in the same rule as in the experiment.

Table 1: Water flow test conditions

Test No.	Tank Pressure	Mass Flow	Mass Flow	Move Solenoid Valve	Sampling Rate		NOTE
	PT	q_1	q_2		Omni-Ace	FBG	
	[MPaG]	[g/s]	[g/s]		[Hz]	[Hz]	
Test-01	2	18.0	18.0	SV1, SV2	10000	1000	Normal Mode ※1, 2
Test-02	2	18.0	-	SV1	10000	1000	SV2 Anomaly Mode ※2
Test-03	2	-	18.0	SV2	10000	1000	SV1 Anomaly Mode ※2
Test-04	2	18.0	18.0	SV1, SV2	10000	1000	Normal Mode (L part configuration change) ※2
Test-05	2	18.0	18.0	SV1, SV2	10000	1000	Air bubble localization Mode (L part configuration change) ※2
Test-06	2	18.0	18.0	SV1, SV2	10000	1000	Normal Mode (T part configuration change) ※2
Test-07	2	18.0	18.0	SV1, SV2	10000	1000	Air bubble localization Mode (T part configuration change) ※2

※1. Normal mode was tested for reproducibility five times under the same conditions (100 ms ON/300 ms OFF×3 pulses).

※2. Duty (100 ms ON/300 ms OFF, 62 ms ON/63 ms OFF, 50 ms ON/150 ms OFF, 20 ms ON/60 ms OFF, 160 ms ON/40 ms OFF) ×3 pulses.

DOI: 10.13009/EUCASS2022-6177

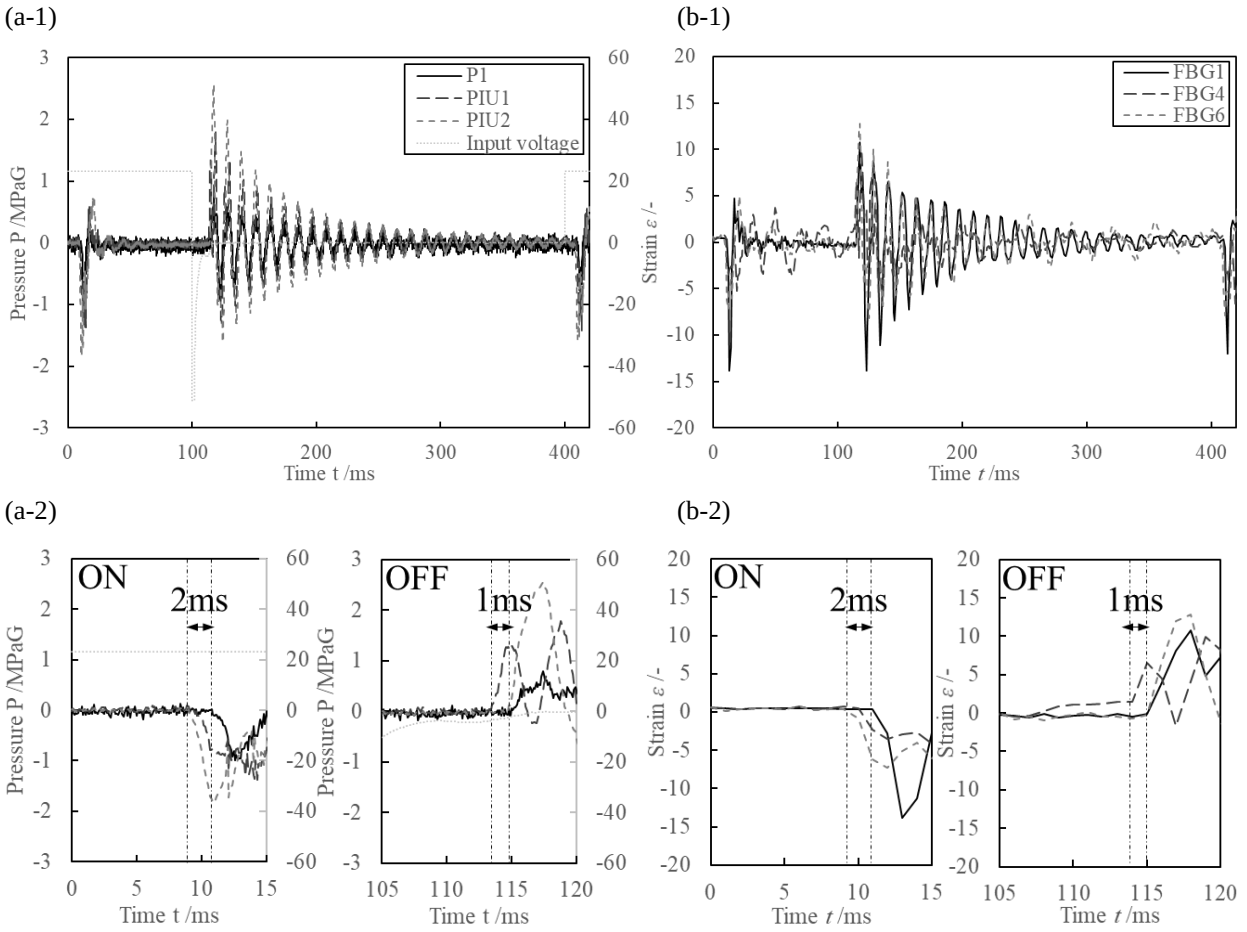

Figure 2: Comparison of pressure and strain changes measured by pressure sensor and FBG during solenoid valve ON/OFF (1 pulse: 0–420 ms). (a-1): Measured pressure and input voltage at solenoid valve ON/OFF (1 pulse). (a-2): Enlarged view of measured pressure and input voltage at solenoid valve ON/OFF (1 pulse). (b-1): Measured strain at solenoid valve ON/OFF (1 pulse). (b-2): Enlarged view of measured strain at solenoid valve ON/OFF (1 pulse)

3. Result

The output results during the water hammer response were confirmed. Figure 2 shows the output results of the pressure and strain time-series data of Test-01 (normal mode) at Duty: 100 ms ON/300 ms OFF. P1, PIU1, PIU2, FBG1, FBG4, and FBG6 are shown as representative pressure and strain time-series data. As shown in Figure 2(a-1), we confirmed that the initial pressure was 2 MPaG as set by the pressure sensor measurement results. Next, we confirmed that the solenoid valve drive voltage turned ON at t = 0 ms, OFF at t = 100 ms, and ON again at t = 400 ms. On the other hand, the time-series data of the pressure shows the response of the solenoid valve opening at 8 ms, the response of the solenoid valve closing at 110 ms, and the response of the solenoid valve opening again at 408 ms. Therefore, it was confirmed that the open state time is 02 ms for an ON time of 100 ms, and the close state time is 298 ms for an OFF time of 300 ms. On the other hand, the strain time-series data obtained by the FBGs (FBGs 1, 4, and 6) shown in Figure 2(b-1) similarly show the solenoid valve open response at 10 ms, solenoid valve close response at 112 ms, and solenoid valve open response again at 410 ms, indicating that the open state time is 102 ms, and the close state time is 298 ms. Therefore, it was found that the response was captured at the same level with an open state time of 102 ms and a close state time of 298 ms.

Next, to confirm that the differences in the water hammer response time at the downstream PIU1 (FBG4) and PIU2 (FBG6) and upstream P1 (FBG1) positions are consistent, we compared the solenoid valve opening and closing times in Figures 2(a-2) and (b-2). Figures 2(a-2) and 2(b-2) demonstrate a slight individual difference in the open/close time between solenoid valves SV1 and SV2, and that the difference in the solenoid valve open/close time is 1 ms. The pressure fluctuation generation time when the solenoid valve was opened showed that PIU1 and

DOI: 10.13009/EUCASS2022-6177

PIU2 responded almost simultaneously, and P1 was delayed by 2 ms. The trend was similar for FBGs, with FBG6 and FBG4 responding simultaneously and FBG1 being delayed by 2 ms. On the other hand, at the solenoid valve closing time, PIU2 responded, followed by PIU1 and P1 responses in 1 ms, and similarly for FBG, FBG6 responded, followed by FBG4 and FBG1 responses in 1 ms. Therefore, the difference in pressure response time between the measurement positions was almost the same for the pressure sensor and FBG.

From these time-series data of strain, the following three points should be discussed to clarify the applicability of an anomaly detection method using multiplexed FBGs with multipoint correlation. The first point is to evaluate the accuracy of acquisition data by comparing the pressure converted from the FBG strain with the pressure sensor at the equivalent position. Also, the same evaluation should be performed where pressure sensors are not installed, using the calculated values calculated from the analytical model. These results confirm the utility of FBG as a sensor. The second point is to extract the pressure response characteristic quantities depending on the flow rate anomaly and the air bubble localization. By examining whether the time-series data and frequency characteristics have characteristic quantities that can determine anomaly conditions, we can clarify the characteristic quantities that should be compared to see the subsequent correlation among multiple points. The third point is the proposal and verification of anomaly detection algorithms. This clarifies whether the algorithm can detect each anomaly and state change and the possibility of identifying anomalous sections.

4. Discussion

4.1. Accuracy evaluation of acquiring water hammer pressure characteristics

4.1.1. Accuracy evaluation of FBG strain acquisition by comparison with actual pressure measurements

The FBG strain data obtained from the tests were converted to the internal pressure of the pipe using the strain-pressure relationship (2), assuming that the pipe is a thick-walled cylinder. This model uses Young's modulus E, Poisson's ratio v, inner diameter R_i, and outer diameter R_o to convert strain ε to pressure. The obtained pressure is the differential pressure ΔP_{FBG} from the start of the strain measurement since the zero point of the strain is set at the start of the measurement.

$$\Delta \boldsymbol{P_{FBG}} = \frac{\boldsymbol{E}}{\boldsymbol{2(1-v)}} \frac{\boldsymbol{R_o^2 - R_i^2}}{\boldsymbol{R_i^2}} \boldsymbol{\varepsilon} \tag{2}$$

Figure 3 compares the time-series differential pressure ΔP_{FBG}, which is the strain measured by the FBG converted to pressure, and the measured differential pressure ΔP_P of the pressure sensor with the initial pressure of 2.0 MPaG as the zero point (0 MPaG). As an example, comparing the values of ΔP_{FBG} and ΔP_P calculated by FBG1 with 90° attachment and FBG6 with 45° attachment, FBG1 and P1 shown in Figure 3(a) have a small error of 0.89% in the maximum water hammer pressure against the pressure time-series data from the pressure sensor. However, FBG6 and PIU2 had a large discrepancy in the error of the maximum water hammer pressure, 23%.

Here, to obtain the absolute pressure values more precisely, it is necessary to make corrections according to the installation angles of the FBGs. As described in section 2.1, the installation angles in this research are 90° to the direction of fluid flow for FBG1 with 1/2" piping and 45° to the direction of fluid flow for FBG6 with 1/4" piping. However, the measured installation angles were 87.2° and 52.3° for FBG1 and 6, respectively. The target attachment angle of 90° was accurate within 3%, while the attachment error of 45° had a larger error of 16%. Therefore, it is necessary to correct these attachment angles based on the angles measured after attachment. When the correction of the measured angles is included, Equation (2) is expressed by Equation (3).

$$\Delta \boldsymbol{P_{FBG}} = \frac{\boldsymbol{E}}{\boldsymbol{2(1-v)\cos(90-\theta)}} \frac{\boldsymbol{R_o^2 - R_i^2}}{\boldsymbol{R_i^2}} \boldsymbol{\varepsilon} \tag{3}$$

The time-series data of the measured strain-converted differential pressure obtained using Equation (2) and the time-series data of the pressure sensor are shown in Figure 3(b). Comparing the maximum water hammer pressure of ΔP_{FBG} with ΔP_P, the error was 1% for FBG1 with 90° attachment and 3% for FBG6 with 45° attachment,

DOI: 10.13009/EUCASS2022-6177

which was a reduction of error compared to the conversion results (Figure 3(a)) obtained with Equation (2) without considering attachment angle error. Therefore, the maximum water hammer pressure error can be reduced from the value of the differential pressure ΔP_P measured by the pressure sensor by using Equation (2) to convert the strain to pressure assuming a thick-walled cylinder.

An FFT (Fast Fourier Transform) was performed on each time-series data of ΔP_{FBG} converted from the FBG measured strain and ΔP_P measured by the pressure sensor in the 400 ms interval from the time of solenoid valve ON to the ON time of the next pulse. The accuracy of obtaining the natural frequency of water hammer pressure response shown in Figure 4 was evaluated. To eliminate noise, a high-pass filter up to 70 Hz was applied to the time-series data. To facilitate the comparison of relative intensities, normalization was performed by dividing the power spectral density I for all frequencies by the maximum value I_{max} of the power spectral density of the pressure sensor and FBG. Comparing FBG1 and P1 shown in Figure 4(a), it is seen that the frequency response characteristics of this test system have three I/I_{max} peaks in the water hammer pressure response. Among these peaks, peak I_1 at 88 Hz showed the maximum intensity, which is considered to represent the natural frequency from the tank to the solenoid valve due to the internal fluid sound velocity in this test.

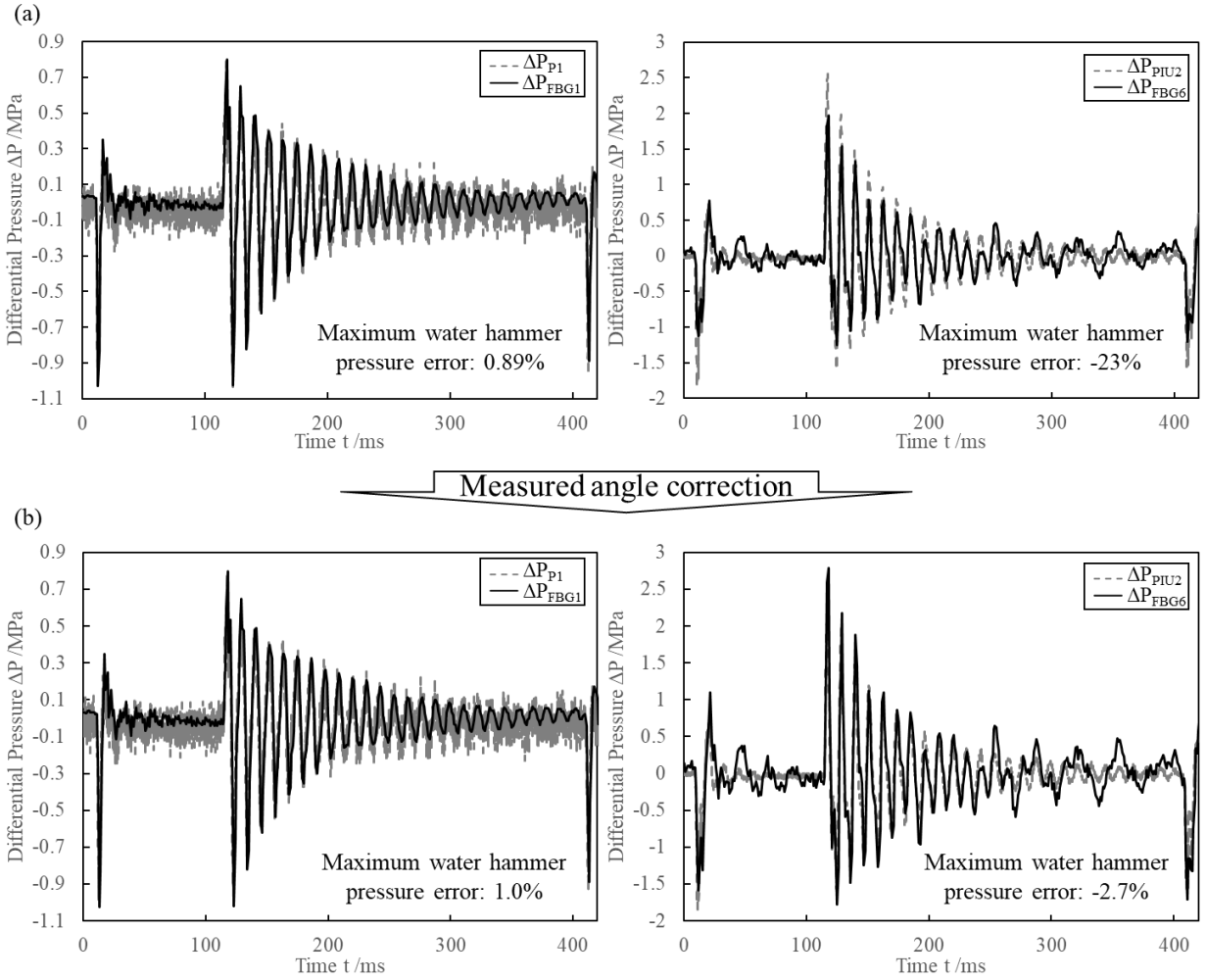

Figure 3: Comparison of FBG and pressure sensor differential pressure time-series data (0–420 ms). (a) The upper two figures show the comparison results of differential pressure converted by Equation (2) without including the measured angle correction. (b) The lower two figures show the comparison results of differential pressure converted by Equation (3), including the measured angle correction.

DOI: 10.13009/EUCASS2022-6177

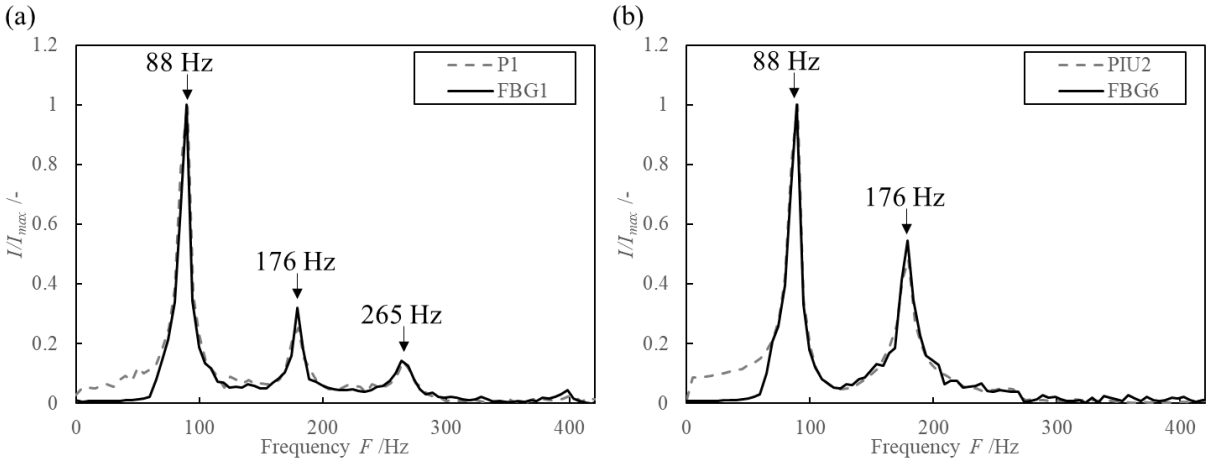

Figure 4: Comparison of frequency response characteristics of time-series data of measured differential pressure and FBG strain-converted differential pressure at water hammer occurrence (0–400 ms).

The peaks at 176 Hz and 265 Hz are thought to be caused by pressure waves reflected from the solenoid valve at its attachment to the small-diameter pipe since there is large-diameter piping upstream of the solenoid valve in this system. The peak frequencies of FBG1 and P1 coincided at the peak I_2 of 176 Hz and the peak I_3 of 265 Hz, with a precision of 1%. Furthermore, as shown in Figure 4(b), when FBG6 and PIU2 at the same position are also compared, the natural frequency peak I_1 is 88 Hz, which is consistent with the results of FBG1 and P1, and has the maximum intensity, confirming that it is the natural frequency of the pipeline in the water hammer pressure response. Furthermore, both FBG6 and PIU2 have an intensity peak (error less than 1%) at the peak I_2 at 176 Hz but not at the peak I_3 at 265 Hz. Therefore, FBGs can acquire natural frequencies to the same degree as pressure sensors.

4.1.2. Accuracy evaluation of FBG measurement at bifurcation using analytical model

The analytical model was tuned by comparing the water hammer response pressure of FBG1 obtained in this experiment with that of the analytical model simulating the piping system in this test. In this model, the volume modulus in the theoretical equation for fluid sound velocity was adjusted, and the primary mode's natural frequency (88 Hz) was adjusted so that the error was within 1%. The theoretical equation for the sound velocity C is expressed as follows

$$C = \sqrt{\frac{E}{\rho}} \tag{4}$$

E is the bulk modulus and ρ is the density. The density ρ is substituted for the literature value [8], and only the bulk modulus E is adjusted. A comparison of one pulse of the water hammer pressure response obtained in normal operation (Test-1) is shown in Figure 5. First, in Figure 5(a), the calculated maximum water hammer differential pressure is 0.92 MPa, which agrees with the measured values within 20%. The reason for the error between the analysis and measured maximum water hammer pressure is considered the solenoid valves do not open and close completely at the same time. Comparing the frequency response characteristics in Figure 5(b), the frequencies of I_1, I_2, and I_3 agree with errors of 1%, 5%, and 5%, respectively. Therefore, the water hammer response characteristics of the analytical model are highly reproducible for this study. The sound velocity of the analytical model obtained by Equation (4) is 1450 m/s, which is close to the theoretical sound velocity of pure water at 25°C, 1498 m/s [8], and the validity of the model is also confirmed.

Based on the calculated values obtained from the analytical model and the results of the model evaluation using the measured values of the pressure sensors, the accuracy of the FBG measured pressure at locations where no pressure sensors were installed was evaluated. Figure 6 compares the water hammer pressure response at a location

DOI: 10.13009/EUCASS2022-6177

close to FBG2 obtained using the analytical model and the measured FBG2 values. First, in Figure 6(a), the time-series data of FBG2 under normal conditions are compared with the calculated values. It is confirmed that the calculated maximum water hammer differential pressure is 1.06 MPa, which agrees with the measured values within 22%. In addition, comparing the frequency response characteristics in Figure 6(b), the frequencies of I_1, I_2, and I_3 agreed with the values measured by FBG2 with an error of less than 1% and 5%, respectively. These test data of the simulated flow rate anomaly (totally closed failure) were compared, and the characteristic result satisfies the result of the model evaluation that the frequency error at I_2 is within 5%. Therefore, it was found that the accuracy of the FBG measurements is reasonable using the analytical model even in areas with no pressure sensors, such as a T-junction.

4.2. Water hammer characteristics change with normal/anomaly flow rate and with/without bubbles

Changes in water hammer characteristics due to a flow rate anomaly were extracted. The strain-converted differential pressure ΔP_{FBG1} and the frequency characteristics of FBG1 are shown in Figure 7(a) when the flow rate anomaly is simulated (SV2, 0%; SV1, 0%). When the flow rate was set to 0% on the SV2 side, the maximum water hammer pressure decreased by 19%, and when the flow rate was set to 0% on the SV1 side, the maximum water hammer pressure decreased by 37%. Next, comparing the frequency response characteristics, we found that the I_3 intensity ratios differed significantly. When SV1 was assumed to be a closed failure, the intensity ratio at I_3 was the smallest at 0.04.

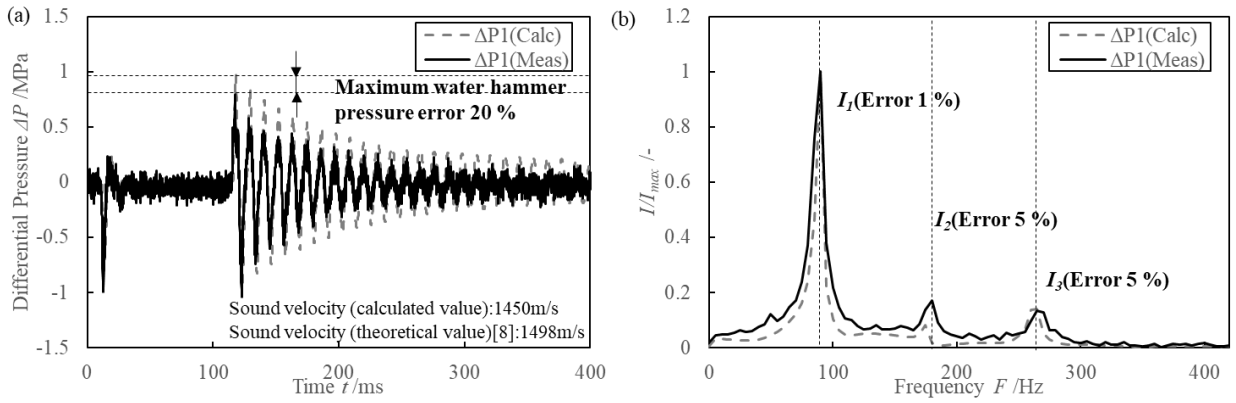

Figure 5: Comparison of calculated values of the analytical model and measured pressures. (a) Comparison of time-series data of pressure (0–400 ms). (b) Comparison of frequency response characteristics of pressure intensity.

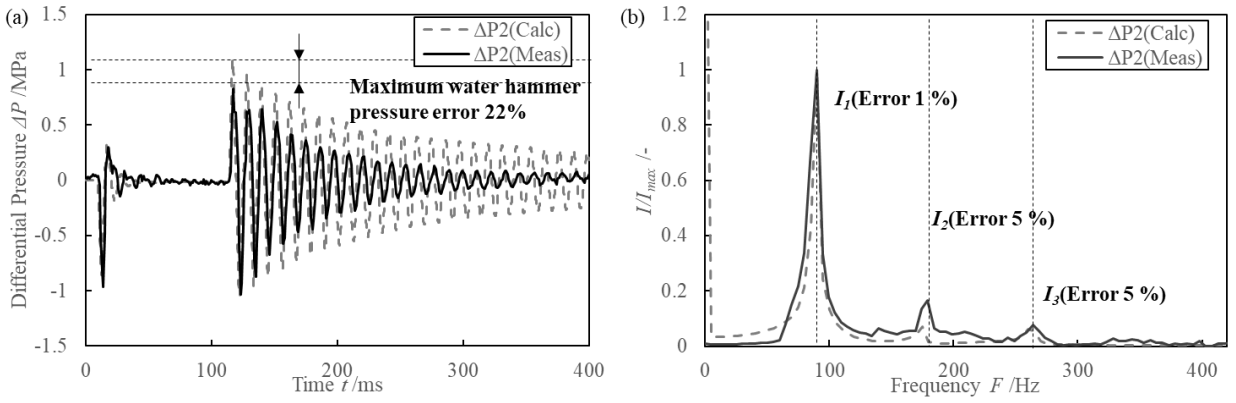

Figure 6: Comparison of calculated values of the analytical model and measured values of FBG2 near the pipe branch point. (a) Comparison of time-series data of differential pressure (0–400 ms). (b) Comparison of frequency response characteristics of I/I_{max}.

DOI: 10.13009/EUCASS2022-6177

However, the I_3 intensity ratio increased significantly during the SV2 closed failure, reaching a maximum intensity ratio of 0.32 at I_3. Therefore, it was confirmed that the change in frequency response characteristics due to flow rate changes could be used to detect flow rate anomalies.

Next, we compared the test data with and without bubble localization and extracted the characteristic changes in the water hammer characteristics. Figure 7(b) shows the strain-converted differential pressure time-series data ΔP_{FBG1} and frequency characteristics of FBG1 for the test simulation with and without bubble localization at the T-junction. Comparing the pressure waveforms, a change in which the natural frequency decreases was observed in the presence of localized bubbles. This is due to the reduction of the apparent sound velocity by the presence of bubbles. In addition, compared to the maximum water hammer pressure, the localization of bubbles results in a reduction of the intensity by 20%. Next, comparing the frequency response characteristics in FBG1, the natural frequency peak I_1 was reduced by 10 Hz, as is clear from the above time-series data. In terms of I_2 and I_3, the frequency of I_2 was consistent at 174 Hz regardless of the presence or absence of bubbles, while the frequency of I_3 increased by 25 Hz with respect to that of the bubble-free state. As for FBG1, similarly to FBG6, the frequency of I_1 was reduced by 10 Hz, while the frequency of I_1 remained almost unchanged. Therefore, the presence or absence of air bubbles indicates a change in the peak frequency, enabling us to detect bubbles' localization. Since the frequency response characteristics can capture the features of anomalies and states, we considered that the FRF be used to capture the correlation among FBGs to capture anomalies and state changes.

4.3. Anomaly detection in the system using frequency response function (FRF)

Based on the results of the studies up to section 4.2, we considered that an anomaly or change in the system could be detected from changes in the correlation function of the measured data among multiple points as an anomaly detection method that takes advantage of the fact that FBGs are installed at multiple points (6 points in total). Therefore, we attempted to apply the FRF as a function that well represents the correlation. The following procedure calculates the FRF. First, the FRF $H(f)$ is expressed by Equation (5) using the Fourier spectrum $A(f)$ of the input signal "a" and the Fourier spectrum $B(f)$ of the output signal "b."

$$\boldsymbol{H(f) = \frac{B(f)}{A(f)}} \tag{5}$$

By multiplying the denominator and numerator on the right side of Equation (5) by the complex conjugate of $A(f)$, $H(f)$ can be expressed as in Equation (6) using the power spectral density $Gaa(f)$ of the input signal "a" and the cross-spectral density $Gba(f)$ between the input signal "a" and the output signal "b".

$$\boldsymbol{H(f) = \frac{B(f) \times A^*(f)}{A(f) \times A^*(f)} = \frac{G_{ba}(f)}{G_{aa}(f)}} \tag{6}$$

Therefore, the gain of the FRF $F(f)$ is given by Equation (7).

$$\boldsymbol{F(f) = 20 \log |H(f)|} \tag{7}$$

$F(f)$ was compared between normal and anomaly conditions to determine the index of anomaly and the threshold value. The calculation range of $F(f)$ was set to the measurement time of three pulses (1200 ms). In this study, to detect correlation changes in each interval, the analysis was divided into (1) correlations of FBGs 1 and 2, (2) correlations of FBGs 2 and 3, (3) correlations of FBGs 3 and 4, and (4) correlations of FBGs 5 and 6. The relationship between the frequency f and FRF gain $F(f)$ calculated by the above Equation (7) is shown in Figure 8. Comparing the results for normal operation, the shapes of $F(f)$ are almost the same for each section.

DOI: 10.13009/EUCASS2022-6177

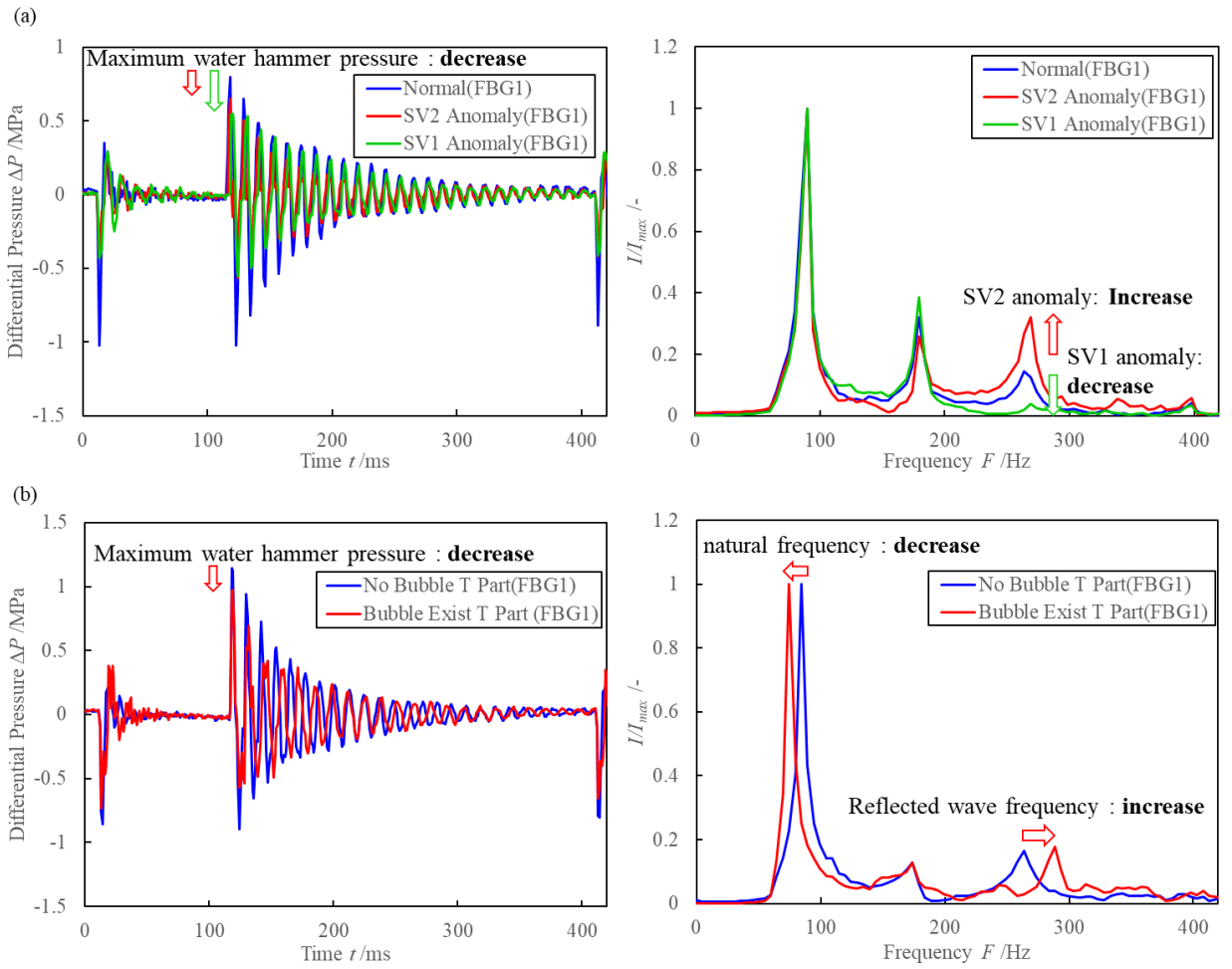

Figure 7: Comparison of differential pressure time-series data and frequency response characteristics under normal and anomaly conditions (flow anomaly, bubble localization). (a) Comparison of time-series data of differential pressure and frequency response characteristics at normal, SV2 anomaly, and SV1 anomaly conditions (0–400 ms). (b) Comparison of time-series data of differential pressure and frequency response characteristics at no bubble T part and bubble exist T part conditions (0–400 ms).

This tendency was also true for the other three conditions where the reproducibility was checked under the same conditions. Based on these results, we considered that the degree of agreement of F(f) could be used as an indicator of anomaly detection, and we used the mean squared error δ_{MSE} as an indicator of anomaly. We compared the δ_{MSE} for each normal operation, the value is less than 5. Therefore, we set the threshold value of $\delta_{MSE} = 10$, which is twice the maximum value of δ_{MSE} in normal operation.

To confirm that the characteristics of $F(f)$ are independent of the solenoid valve opening/closing mode, the relationship between the FRF gain and the frequency for each solenoid valve opening/closing mode is shown in Figure 9 for the SV2 flow anomaly condition. It was confirmed that the trends of FRF gains for each valve opening/closing mode are the same. Because of the high-pass filter at 70 Hz, there is a divergence in the FRF gains for each mode below 70 Hz. However, comparing the normal and anomaly condition of each mode, the FRF gains below 70 Hz remain unchanged, which does not affect δ_{MSE} in judging normal and anomaly. Since there is a slight variation in the relationship between frequency and FRF gain in each mode, it is considered that spectral averaging over all solenoid valve open/close modes is effective in calculating a reliable δ_{MSE}.

Based on the above studies, we confirmed the feasibility of the anomaly detection method. Using $\overline{G_{ba}}$ and $\overline{G_{aa}}$ averaged over all solenoid valve open/close modes, $F(f)$ was calculated from Equations (6) and (7). First, the relationship between the frequency and FRF gain for the flow anomaly during normal operation (normal) and during SV2 and SV1 anomalies (anomaly) are shown in Figures 10(a) and 10(b). FBGs 3 and 4 were slightly above

DOI: 10.13009/EUCASS2022-6177

the threshold value of δ_{MSE}, indicating that there was little anomaly. On the other hand, FBG 2 and 3 and 5 and 6 have δ_{MSE} Values 1.7 times higher than the threshold value, indicating that the correlation between the normal and the sensor is significantly different. Therefore, it is considered that FBGs 2 and 3, and 5 and 6 may be the main failure sections. The above trend is correct since the SV2 failure near FBG6 is simulated. The detected anomalies were in FBGs 1and 2, 2 and 3, and 3 and 4. The δ_{MSE} was 1.5 to 2 times larger than the threshold value in all the sections detected as anomaly, indicating that the correlation between normal and sensors was significantly different. On the other hand, FBGs 5 and 6, whose δ_{MSE} was 1.7 times the threshold value when SV2 was inoperative, have $\delta_{MSE} = 2.96$, which is within the range of normal operation. Therefore, it is considered that the failure intervals of FBGs 1 and2, 2 and 3, and 3 and 4 may be the main failure intervals. The above trend is correct since it simulates the failure of SV1 near FBG4.

Next, Figures 11(a) and 11(b) show the relationship between frequency and FRF intensity in the case of normal operation without bubbles and with bubbles locally introduced into the pipe. First, when bubbles were introduced into the L-shaped bifurcation (between FBGs 5 and 6), anomaly were detected in the sections between FBGs 3 and 4 and between FBGs 5 and 6. Among the detected anomalies, $\delta_{MSE} = 19.5$ for FBGs 3 and 4 and $\delta_{MSE} = 112.7$ for FBGs 5 and 6, showing a large discrepancy in the degree of anomaly. When bubbles were introduced into the T-junction (between FBGs 2 and 3), anomalies were detected at FBGs 2 and 3, 3 and 4, and 5 and 6. Among the detected anomalies, $\delta_{MSE} = 19.4$ for FBGs 2 and 3, $\delta_{MSE} = 69.3$ for FBGs 3 and 4, and $\delta_{MSE} = 36.8$ for FBGs 5 and 6, showing a large discrepancy in the degree of anomaly. Therefore, a large anomaly is considered to have occurred in the interval of FBGs 3 and 4. However, since bubbles were introduced in the interval of FBGs 2 and 3, it would be difficult to capture changes in FRF intensity in such a comparison of very short intervals of 110 mm due to the small changes in the characteristics. Therefore, we believe it would be an effective means to facilitate the detection of anomalies by conducting measurements at locations where there are systematic changes, such as between other measurement points, branch pipes, main pipes, and even changes in pipe diameter.

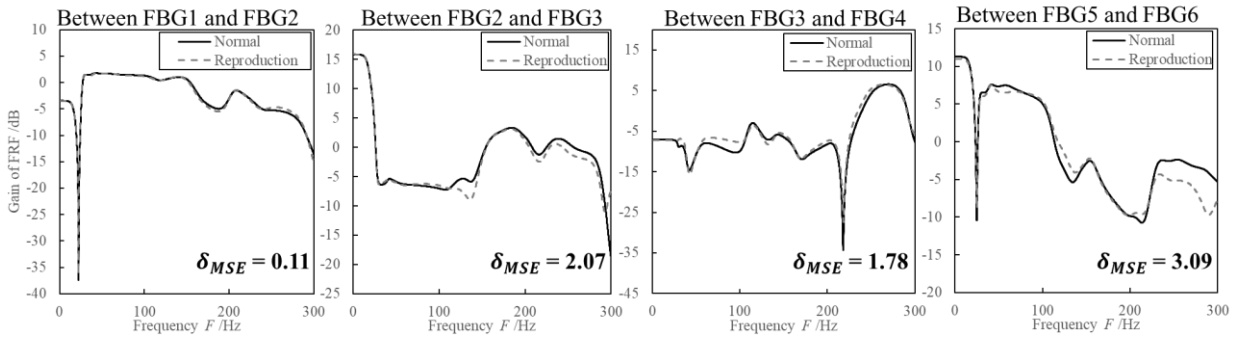

Figure 8: Relationship between frequency and FRF gain obtained from the correlation of two points in each section (normal mode, duty ratio: 100 ms ON/300 ms OFF).

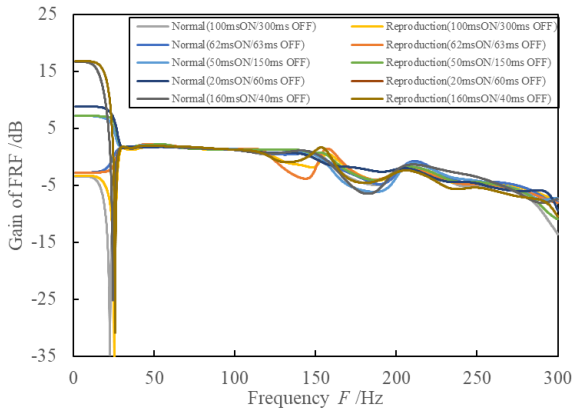

Figure 9: Relationship between frequency and gain of FRF between FBGs 1 and 2 in the normal mode.

DOI: 10.13009/EUCASS2022-6177

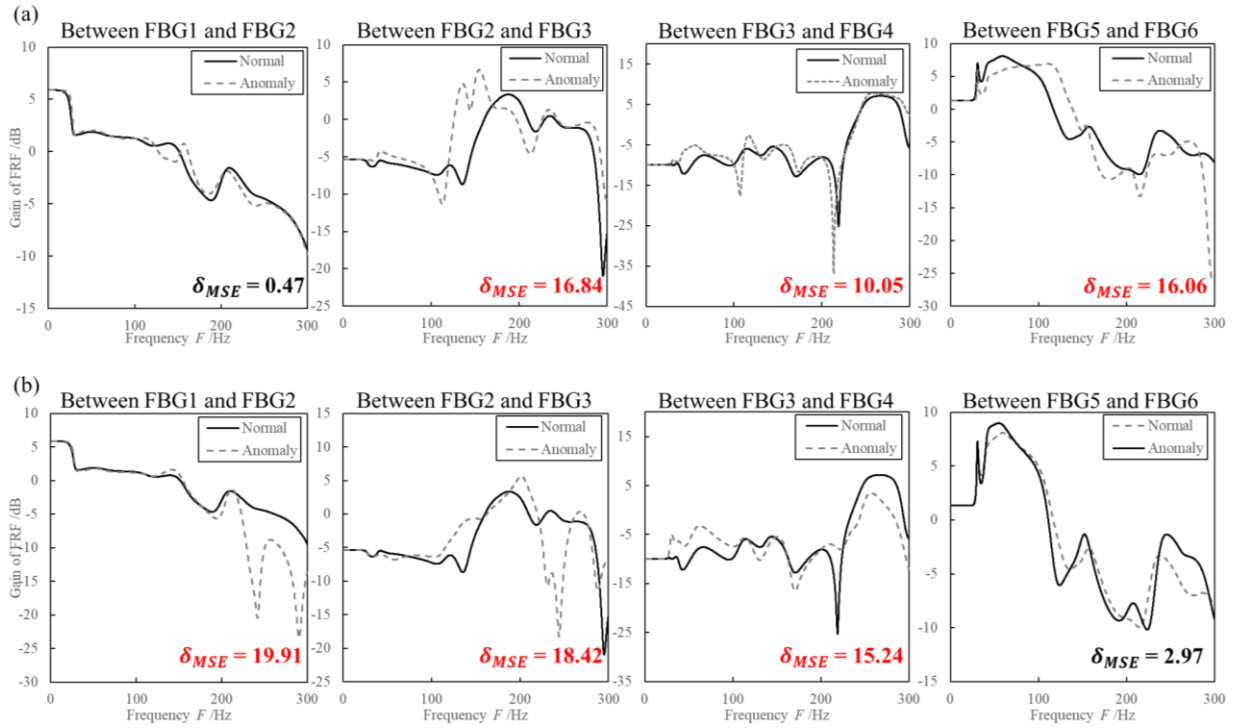

Figure 10: Relationship between frequency and FRF gain under normal and anomaly flow conditions. (a) Result of Least-squares error calculated by FRF comparison between normal and SV2 anomaly conditions. (b) Result of least-squares error calculated by FRF comparison between the normal state and SV1 anomaly condition.

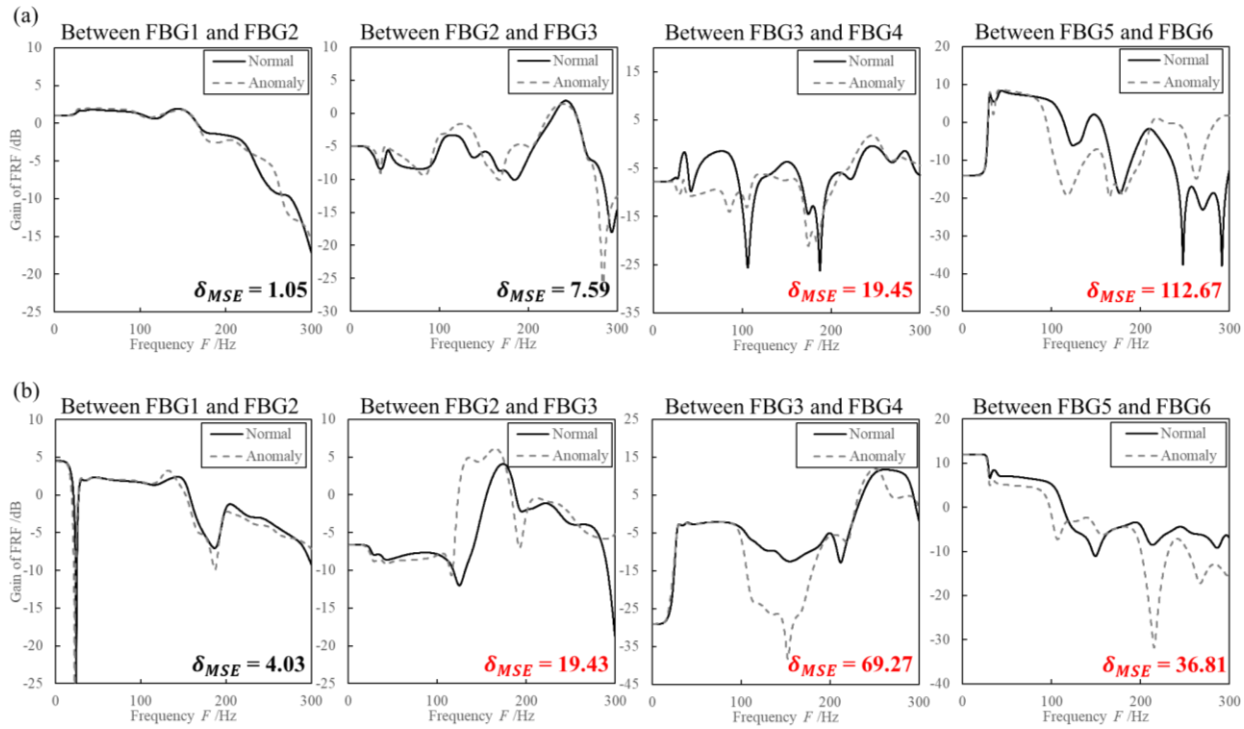

Figure 11: Relationship between frequency and FRF gain under normal and bubble localization conditions. (a) Result of Least-squares error calculated by FRF comparison between normal and bubble localization (L part) condition. (b) Result of least-squares error calculated by FRF comparison between the normal state and bubble localization (T part) condition.

DOI: 10.13009/EUCASS2022-6177

5. Conclusion

This study aims to clarify a method to detect anomalies using multiplexed FBGs with multipoint correlation. The following findings were obtained by evaluating the accuracy of pressure acquisition by strain measurement using FBG and by performing anomaly detection using FRFs between two FBG points.

1. Realization and verification of an innovative pressure measurement by optical fiber attachment to narrow pipes of a spacecraft propulsion system.

✓ Narrow pipe strain due to water hammer was measured using FBGs attached around pipe at an incline to reduce light loss due to steep bending. The narrow pipe strain can be converted to pressure using a thick-walled cylindrical model with a measured angle correction, which enables pressure acquisition with a maximum water hammer pressure error of 2% and an accuracy of within 1% of the I/I_{max} peak error in natural frequency with respect to the measured pressure at the same position.

✓ Even in areas where pressure sensors are not installed, it is possible to obtain pressure with an error of 20% of the maximum water hammer pressure compared to the calculated pressure obtained from the analytical model and with an error of 5% or less for the I/I_{max} peak frequency.

2. Study and trial approaches to anomaly detection based on measurement data obtained by the above measurement methods

✓ Flow anomaly in the system causes a significant change in the intensity ratio of the reflected wave in the relation between frequency and power spectrum, and bubble localization has a change in the characteristic quantities of decrease in natural frequency and increases in the frequency of the reflected wave regarding the dynamic response which may be affected by change of the sound velocity in propellant due to trapped gas.

✓ The mean-square error of the frequency response function obtained from any two points during normal and anomaly operation (anomaly flow rate, bubble localization) can be used to detect anomalies. Furthermore, the magnitude of the frequency response function can be used to estimate the section where the anomaly occurs.

References

[1] K. Kawatsu, C. Inoue, Y. Terauchi, Y. Daimon, G. Fujii, and A. Noumi. 2019. System-level Integrated Modeling and Simulation Targeting Space Propulsion System for Design Evaluation and Risk Assessment. *32nd International Symposium on Space Technology and Science*, 2019-a-96-103.

[2] K. Kawatsu, A. Noumi, N. Ishihama, T. Nagata, C. Inoue, G. Fujii, H. Tani, and Y. Daimon. 2020. Resilient Redundant Spacecraft GN&C System Fault Detection and Diagnostics. *Aerospace Europe Conference 2020*. AEC2020_467-463.

[3] G. Fujii, K. Kawatsu, Y. Daimon, K. Michigami, K. Kushiki, S. Sawai, and S. Sakai. 2021. Verification of the Transient Behavior of the SLIM Propulsion System (Smart Lander for Investigating Moon). *AIAA Propulsion and Energy 2021 Forum*, AIAA 2021-3582-3592.

[4] S. T. Vohra. 1999. Fiber Bragg Grating Sensor System for Civil Structure Monitoring: Application and Field Tests. *Technical Digest of 13thInternational Conf. On Optical Fiber Sensors*. SPIE 3746. 30-35.

[5] K. Saruta, K. Tsukimori, Y. Shimada, A. Nishimura, and T. Kobayashi. 2010. Development of a Health Monitoring System Using Thermally Stable Fiber Bragg Gratings for Fast Reactor Power Plants: Experimental Demonstration of Strain Measurement. *JAEA Conf. 2010*. 149-152.

[6] H. Fukushima, M. Wakahara, T. Nishikawa, T. Fukasawa, and T. Kanai. 2015. Hull Surface Pressure Measurement of the Affix-type Multipoint Pressure Sensor using FBG. *Conference proceedings, the Japan Society of Naval Architects and Ocean Engineers*. 21. 327-332.

[7] R. Masui, K. Fujii, and M. Takenaka. 1995. Determination of the Absolute Density of Water at 16℃ and 0.101325MPa. Metrologia. 32. 333-362.

[8] M. Greenspan, and C. E. Tschiegg. 1957. Speed of Sound in Water by a Direct Method", Journal of Research of the National Bureau of Standards. 59. 4. 249-254.